PAPER

A phase-transition model of reprocessible thermadapt shape memory polymer

To cite this article: Tong Mu *et al* 2024 *Smart Mater. Struct.* **33** 045007

IOP Publishing Smart Materials and Structures
Smart Mater. Struct. **33** (2024) 045007 (11pp) https://doi.org/10.1088/1361-665X/ad2c72

A phase-transition model of reprocessible thermadapt shape memory polymer

Tong Mu[1], Fei Jia[2], Wei Zhao[2], Yanju Liu[2] and Jinsong Leng[1,*]

[1] Center for Composite Materials and Structures, Science Park of Harbin Institute of Technology (HIT), PO Box 3011, No. 2, YiKuang Street, Harbin 150080, People's Republic of China
[2] Department of Astronautical Science and Mechanics, Harbin Institute of Technology (HIT), PO Box 301, No. 92 West Dazhi Street, Harbin 150001, People's Republic of China

E-mail: lengjs@hit.edu.cn

Received 9 September 2023, revised 2 February 2024
Accepted for publication 21 February 2024
Published 7 March 2024

Abstract

A new type of thermadapt shape memory polymer (SMP) has not only the processability of thermoplastic SMP, but also the excellent shape fixation of thermosetting SMP. To enhance the application of this thermadapt SMP within industrial sectors, a comprehensive constitutive model based on phase transition is being proposed as an indicative descriptor of the semi-crystalline thermadapt SMP's salient features, predominantly related to its two-way shape memory effect (SME) and thermal reprocessability. The concept of cooling elongation is also introduced in this model for modeling the two-way SME during the crystallization process. The molecular mechanism of chain-packing has been studied and used to establish phenomenological formulas. In addition, to systematically assess the temperature-time dependence of the crystallization process, the Avrami equation is improved by incorporating the distribution of polymer chain segments. This strategy provides a detailed investigation into the evolving pattern of the crystallization process in response to various temperature and time conditions. Compared with the experimental results, it is found that our model can well capture mechanical behavior in multiple shape memory cycles, including the two-way SME and reshaping process caused by bond exchange reaction. Furthermore, the potential application of SMP in smart mandrels is explored because the cooling elongation feature is able to endow it with self-adaptive expansion ability.

Keywords: shape memory polymer, constitutive model, thermoplastic, vitrimer

1. Introduction

Shape memory polymer (SMP) is a type of smart material that has received widespread attention [1–3]. SMP is capable of fixing temporary shapes and reverting to original shapes, i.e. shape memory effect (SME), where the transition temperature plays an important role in the switching of shape fixing and recovery. The transition temperatures of amorphous and crystalline SMP are related to the glass transition temperature T_g and the melting temperature T_m, respectively. The glass transition is the mechanism for SMPs widely applied to achieve the SME [4–7]. However, some semi-crystalline SMPs crystallize before the glass transition, that is, $T_g < T_m$. At the same time, the SME is caused by the crystalline transition, and its transition temperature is T_m. Semi-crystalline SMP frequently displays unique SMEs, including the two-way SME. This phenomenon implies that the temporary shape of the SMP undergoes a significant transformation correlating with temperature changing during the cooling stage in the SMC.

* Author to whom any correspondence should be addressed.

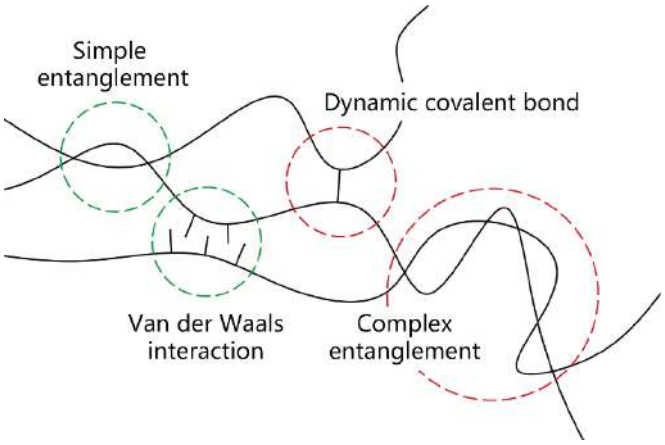

Figure 1. Schematic of four interactions of thermadapt SMP. Red part is fixed in the SMC and the green part is changed.

Hence, semi-crystalline SMP can display two temporary shapes [8–11].

Recently, a new type of polymer containing dynamic covalent bonds (DCBs), known as vitrimer, has attracted widespread research interest [12–14]. By introducing the bond exchange reaction (BER) of DCB, the permanent covalent crosslinking network of thermosetting polymers becomes an equilibrium of breaking and binding. Therefore, the vitrimer exhibits thermoplasticity at higher temperatures. The temperature at which the vitrimer shows significant thermoplasticity is noted as the reaction temperature T_r.

The reaction temperature T_r is normally lower than the melting temperature T_m, the cross-linked network of polymers is in a frozen state, and the original shape of the polymer cannot be changed due to DCB. Zheng *et al* [15] reported a new kind of vitrimer, which is named as thermadapt SMP due to its SME and processability. Compared with normal vitrimer, the reaction temperature T_r of the thermadapt SMP is much higher than its melting temperature T_m. This kind of thermadapt SMP combines the advantages of both thermoplastic and thermosetting SMPs.

Microscopically, the thermadapt SMP [15] is a crosslinking network formed by the interactions among polymer chain segments, such as chemical bonds, secondary bonds or entanglement, as shown in figure 1. When the temperature is higher than the melting temperature T_m, such a crosslinking network spontaneously flows because of entropic elasticity, and then recovers to its original shape. When the temperature drops below T_m, the network is frozen by the strong intermolecular interaction. Therefore, it can be seen that the interactions marked in green in figure 1 will be disrupted in the SMC, while the red parts are permanent. When the temperature exceeds T_r, the original shape can be redefined. As the temperature increases, the DCBs are gradually activated, causing the polymer network to become a dynamic covalent network. The DCB in the SMP network undergoes continuous exchange reactions, causing the network crosslinking points to always be in a dynamic equilibrium of binding and breaking (marked in red in figure 1); thereby the original shape of the SMP can be changed at this temperature.

Available works mainly focus on amorphous thermosetting SMP, while the modeling of thermadapt SMP and crystalline SMP remains to be developed. Several recent studies have reported the modeling of polymer with DCB. Ma *et al* developed a model of photoactivated covalent adaptive networks [16]. In addition, a series of studies have extended this concept to a type of amorphous DCB. However, if the T_r of the investigated polymer is close to the glass transition temperature [17], the model cannot be used directly for thermadapt SMP.

A phase transition model of SMP [18–21] is also adopted for modeling crystalline SMP. Barot *et al* have established a thermodynamic constitutive model for crystalline SMP [22, 23]. Hall *et al* extended the model to the two-way SMP [24]. Westbrook *et al* established a 1D model of infinitesimal deformation to predict the two-way SMC [25].

However, few models consider the crystallization of SMP. Hence, they have some limited to simultaneously predict the SMC and the two-way SME of thermadapt SMP. In this article, a constitutive model of thermadapt SMP between a large temperature range is developed considering crystalline SMC and thermal reprocessing. In section 2, a two-phase constitutive model for thermadapt SMP with a focus on the phase transition process is developed. The Avrami equation is improved for the evolution law of the volume fraction of the crystalline phase. The deformation relationship between different phases during the phase transition is formulated based on a molecular mechanism model, thus establishing the cooling elongation equation used to predict the two-way SMC. In section 3, the model parameters are determined through differential scanning calorimetry (DSC), dynamic mechanical analysis (DMA) and relaxation experiments, and the model is validated by the prediction of the SMC and thermal reprocessing during BER of thermadapt SMP.

2. Modeling

A two-phase model consisting of amorphous and crystalline phases is adopted to develop a constitutive model for describing the thermo-mechanical behavior of a semi-crystalline thermadapt SMP, as shown in figure 2(a). First, a kinematic framework for each phase is adopted enabling the constitutive model to describe the viscoelasticity and thermal expansion of the thermadapt SMP. Second, the elastic relationships of each phase and the whole are established. An evolution law for the volume fraction of the crystalline phase is also developed. Next, a cooling elongation model is developed to study the deformation relationship between the two phases during the phase transition. Finally, a temperature-dependent viscosity

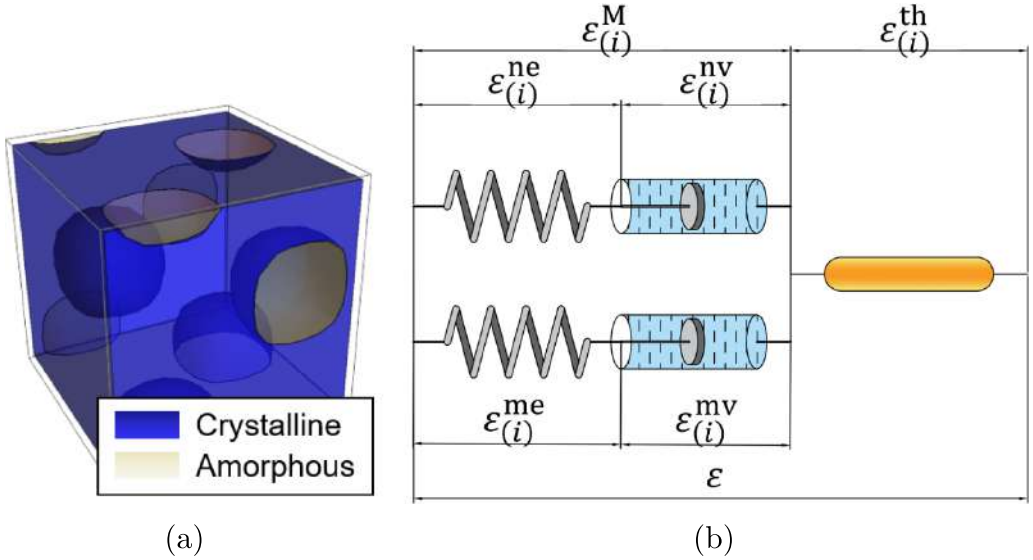

Figure 2. Schematics of the model of the thermadapt SMP. (a) Two-phase model of a microscopic unit of the SMP including the crystalline and amorphous phases. (b) 1D rheology model of the crystalline and amorphous phases under infinitesimal deformation.

flow rule is adopted for the flow of a dynamic covalent network.

2.1. Kinematics

In the two-phase constitutive model, the two phases have the same kinematic characteristics and a five-element model shown in figure 2(b) is used for each phase. The model includes a thermal expansion element and mechanical elements connected in series with it. The mechanical elements are divided into two parallel branches, the intermolecular resistance branch and network branch, respectively. Each branch consists of a series-connected spring element and a dashpot element, representing elastic and inelastic deformations, respectively.

The deformation gradient tensor $\mathbf{F}_{(i)}$ of each phase can be decomposed multiplicatively into tensors of thermal expansion and mechanical deformation:

$$\mathbf{F}_{(i)} = \mathbf{F}^{M}_{(i)}\mathbf{F}^{\mathrm{th}}_{(i)}, \tag{1}$$

where the subscript i represents different phases, $i=a$ for the amorphous phase and $i=c$ for the crystalline phase. $\mathbf{F}^{\mathrm{th}}_{(i)}$ implies the deformation gradient of the thermal part, while $\mathbf{F}^{M}_{(i)}$ implies the deformation gradient of the mechanical part consisting of two parallel Maxwell components, named the network branch and intermolecular resistance branch. The network branch can be further decomposed as,

$$\mathbf{F}^{M}_{(i)} = \mathbf{F}^{ne}_{(i)}\mathbf{F}^{nv}_{(i)}, \tag{2}$$

and the intermolecular resistance branch can be decomposed similarly as,

$$\mathbf{F}^{M}_{(i)} = \mathbf{F}^{me}_{(i)}\mathbf{F}^{mv}_{(i)}, \tag{3}$$

where n and m indicate the network branch and intermolecular resistance branch, while e and v represent the elastic and viscous deformation, respectively. Thus, $\mathbf{F}^{ne}_{(i)}$ and $\mathbf{F}^{nv}_{(i)}$ are the elastic and viscous deformation gradient tensors of the network branch, while $\mathbf{F}^{me}_{(i)}$ and $\mathbf{F}^{mv}_{(i)}$ are the elastic and viscous deformation gradients of the intermolecular resistance branch, respectively.

The determinant of elastic deformation of the network branch is,

$$J^{ne}_{(i)} = \det\left(\mathbf{F}^{ne}_{(i)}\right). \tag{4}$$

The deviatoric deformation gradient, deviatoric right Cauchy–Green tensor, and first invariant of deviatoric right and left Cauchy–Green tensor are defined for the network branch as follows:

$$\begin{aligned}
&\bar{\mathbf{F}}^{ne}_{(i)} = J^{-1/3}_{(i)}\mathbf{F}^{ne}_{(i)}, \quad \bar{\mathbf{C}}^{ne}_{(i)} = \left(\bar{\mathbf{F}}^{ne}_{(i)}\right)^{T}\bar{\mathbf{F}}^{ne}_{(i)},\\
&\bar{\mathbf{b}}^{ne}_{(i)} = \bar{\mathbf{F}}^{ne}_{(i)}\left(\bar{\mathbf{F}}^{ne}_{(i)}\right)^{T}, \quad \bar{I}^{ne}_{(i)} = \mathrm{tr}\left(\bar{\mathbf{C}}^{ne}_{(i)}\right),
\end{aligned} \tag{5}$$

and the variables for the intermolecular resistance branch can be defined in a similar way:

$$\begin{aligned}
&\bar{\mathbf{F}}^{me}_{(i)} = J^{-1/3}_{(i)}\mathbf{F}^{me}_{(i)}, \quad \bar{\mathbf{C}}^{me}_{(i)} = \left(\bar{\mathbf{F}}^{me}_{(i)}\right)^{T}\bar{\mathbf{F}}^{me}_{(i)},\\
&\bar{\mathbf{b}}^{me}_{(i)} = \bar{\mathbf{F}}^{me}_{(i)}\left(\bar{\mathbf{F}}^{me}_{(i)}\right)^{T}, \quad \bar{I}^{me}_{(i)} = \mathrm{tr}\left(\bar{\mathbf{C}}^{me}_{(i)}\right).
\end{aligned} \tag{6}$$

For simplification, the thermal component is isotropic; then its deformation gradient tensor is written as,

$$\mathbf{F}^{\mathrm{th}}_{(i)} = \left(J^{\mathrm{th}}_{(i)}\right)^{1/3}\mathbf{I}, \tag{7}$$

where $\mathbf{I}$ is a second-order unit tensor and the determinant of the thermal component is $J^{\mathrm{th}}_{(i)} = \det(\mathbf{F}^{\mathrm{th}}_{(i)})$. Assuming that the

thermal deformation is linearly proportional to the change in temperature, it gives the following:

$$J_{(i)}^{\mathrm{th}} = 1 + \alpha_i \left(T - T^{\mathrm{ref}}\right), \tag{8}$$

where $\alpha_i (i = a, c)$ are coefficients of thermal expansion of the two phases.

2.2. Elasticity

Within the thermodynamic framework, the Helmholtz free energy density Ψ can be decomposed as,

$$\Psi = \phi_a \Psi_{(a)} + \phi_c \Psi_{(c)}, \tag{9}$$

where ϕ_a and ϕ_c indicate the volume fraction of the amorphous and crystalline phases, respectively. $\phi_a + \phi_c = 1$. $\Psi_{(a)}$ and $\Psi_{(c)}$ are the energy densities of the amorphous and crystalline phases, respectively. Each can be decomposed into three parts, associated with the energy densities of the network branch, intermolecular branch and volume part:

$$\Psi_{(i)}\left(\bar{\mathbf{C}}_{(i)}^{ne}, \bar{\mathbf{C}}_{(i)}^{me}, J_{(i)}^{M}, T\right) = W_{(i)}^{n}\left(\bar{\mathbf{C}}_{(i)}^{ne}, T\right) + W_{(i)}^{m}\left(\bar{\mathbf{C}}_{(i)}^{me}\right) + U_{(i)}\left(J_{(i)}^{M}\right). \tag{10}$$

In order to capture the nonlinear stretch behavior, the widely used eight-chain model of rubber-like material [26] is applied for the network branch, and the energy density $W_{(i)}^{n}$ is,

$$W_{(i)}^{n} = N k_B T \sqrt{n}\left(\beta_c \lambda_c + \sqrt{n} \log\left(\frac{\beta_c}{\sinh \beta_c}\right)\right), \tag{11}$$

where N denotes the crosslinking number of the unit volume, $k_B = 1.38 \times 10^{-23} \mathrm{J\,K^{-1}}$ is the Boltzmann constant and n is the mean number of bonds between two crosslinks. β_c is an intermediate variable:

$$\beta_c = \mathcal{L}^{-1}\left(\frac{\lambda_c}{\sqrt{n}}\right), \quad \lambda_c = \sqrt{\frac{1}{3}\bar{I}_{(i)}^{ne}}, \tag{12}$$

where λ_c is the effective chain stretch. $\mathcal{L}^{-1}(\cdot)$ is the inverse Langevin function, while the Langevin function is $\mathcal{L}(x) = \coth x - 1/x$.

The stiffness of the intermolecular branch is far greater than that of the network branch, and therefore the deformation of the intermolecular branch is relatively small in this model. In addition, the stress–strain relationship of SMP has good linearity at lower temperatures. Thus, the neo-Hookean model is adopted to describe the energy density of intermolecular branch $W_{(i)}^{m}$:

$$W_{(i)}^{m} = \frac{\mu_0}{2}\left(\bar{I}_{(i)}^{me} - 3\right), \tag{13}$$

where μ_0 is the initial shear modulus.

Finally, the elastic energy density of volume part $U_{(i)}$ is,

$$U_{(i)} = \kappa\left(J_{(i)}^{M} - \log J_{(i)}^{M} - 1\right), \tag{14}$$

where κ is the bulk modulus [27].

Assuming that the deformation gradient tensors of the amorphous and crystalline phases are uniform,

$$\mathbf{F} = \mathbf{F}_{(a)} = \mathbf{F}_{(c)}, \tag{15}$$

which is known as the parallel connection model and has been widely used in the phase-transition model for SMP [20, 21].

Referring to the appendix, the total Cauchy stress can be obtained from the free energy density equation (9):

$$\boldsymbol{\sigma} = \phi_a \boldsymbol{\sigma}_{(a)} + \phi_c \boldsymbol{\sigma}_{(c)}, \tag{16}$$

where $\boldsymbol{\sigma}_{(a)}$ and $\boldsymbol{\sigma}_{(c)}$ are Cauchy stresses of the amorphous and crystalline phases, and each can be further decomposed into its deviatoric and hydrostatic parts:

$$\boldsymbol{\sigma}_{(i)} = \mathbf{s}_{(i)} - p_{(i)}\mathbf{I}, \tag{17}$$

where hydrostatic pressure $p_{(i)}$ can be expressed as,

$$p_{(i)} = -\frac{1}{3}\mathrm{tr}\,\boldsymbol{\sigma}_{(i)} = -\frac{\kappa}{J_{(i)}}\left(J_{(i)}^{M} - 1\right). \tag{18}$$

The deviatoric stress $\mathbf{s}_{(i)}$ of each phase is contributed by the network and intermolecular branches:

$$\mathbf{s}_{(i)} = \underbrace{\frac{\mu^{\mathrm{eq}}}{J_{(i)}}\left(\bar{\mathbf{b}}_{(i)}^{ne} - \frac{1}{3}\bar{I}_{(i)}^{ne}\mathbf{I}\right)}_{\mathbf{s}_{(i)}^{n}} + \underbrace{\frac{\mu_i}{J_{(i)}}\left(\bar{\mathbf{b}}_{(i)}^{me} - \frac{1}{3}\bar{I}_{(i)}^{me}\mathbf{I}\right)}_{\mathbf{s}_{(i)}^{m}}, \tag{19}$$

where μ^{eq} is the equivalent shear modulus:

$$\mu^{\mathrm{eq}} = N k_B T \sqrt{n}\frac{\beta_c}{\lambda_c}. \tag{20}$$

2.3. Evolution law of ϕ_c

The volume fraction of crystalline phase ϕ_c is not only temperature-dependent, but also time-dependent.

First, we study the temperature-dependent feature of ϕ_c, which reaches a stable value $\phi_{c\infty}$ at a certain temperature T after a sufficiently long time. Assuming that the long-term crystallization fraction $\phi_{c\infty}$ is determined only by the temperature, it has the following form:

$$\phi_{c\infty} = 1 - \frac{1}{1 + \exp\left(-\frac{T - T_b}{T_a}\right)}, \tag{21}$$

where T_a and T_b are parameters controlling the evolution of the long-term crystallization. In order to describe the dynamic

crystallization ϕ_c in short-term, Doufas *et al* developed a model [28]:

$$\dot{x} = mK^{\mathrm{av}}\left[-\log\left(1-x\right)^{(m-1)/m}\right](1-x)\exp\left(\xi\frac{\mathrm{tr}\,\boldsymbol{\tau}}{G}\right), \quad (22)$$

where $x = \phi_c/\phi_{c\infty}$, K^{av} and m are Avrami parameters. Ahzi *et al* found that the exponential term is negligible for SMPs [29]. The crystallization equation becomes,

$$\dot{x} = mK^{\mathrm{av}}\left[-\log\left(1-x\right)^{(m-1)/m}\right](1-x). \quad (23)$$

However, equation (23) cannot degenerate to the stable long-term solution $\phi_c = \phi_{c\infty}$. In order to include the effect of long-term crystallization, we modify it as follows:

$$\dot{\phi}_c = mK^{\mathrm{av}}\left[-\log\left(\phi_{c\infty}-\phi_c\right)^{(m-1)/m}\right](\phi_{c\infty}-\phi_c). \quad (24)$$

The solution to equation (24) is,

$$\phi_c = \phi_{c\infty} - \exp\left[-\left(K^{\mathrm{av}}t + K_0\right)^m\right], \quad (25)$$

where $K_0 = \left(-\log\phi_{c\infty}\right)^{-1/m}$. When $m = 1$, the solution can be degenerated into the result of Ahzi *et al*

$$\phi_c = \phi_{c\infty} - \exp\left(-\left(K^{\mathrm{av}}t\right)^m\right)\phi_{c\infty}. \quad (26)$$

The rate of crystallization increases rapidly with the decrease in cooling temperature, and so a temperature-dependent Avrami parameter is introduced:

$$K^{\mathrm{av}} = K^{\mathrm{av}}_{\mathrm{ref}}\exp\left(-\frac{T}{T^{\mathrm{av}}_{\mathrm{ref}}}\right), \quad (27)$$

where $K^{\mathrm{av}}_{\mathrm{ref}}$ and $T^{\mathrm{av}}_{\mathrm{ref}}$ are reference values of Avrami parameters.

2.4. Cooling elongation

A phenomenological model considering the atomic packing of polymer chains is established in this section.

Since the stiffness of the network is much lower than that of the intermolecular branch, the effect of the network branch can be neglected, and we only focus on the intermolecular branch. A 1D model of the intermolecular branch under constant stretch stress is shown in figure 3, where an abnormal elongation occurs due to the crystallization of chains along the stretch direction during cooling [18, 19]. At time t, the fraction of crystalline phase is ϕ_c, while the fraction of amorphous phase $\phi_a = 1-\phi_c$. The strain in the amorphous and crystalline phases are $\varepsilon_{(a)}$ and $\varepsilon_{(c)}$, respectively. If the original length of the chain is L, the increment length of the chain under deformation is,

$$\Delta L = \Delta L_{(c)} + \Delta L_{(a)}, \quad (28)$$

where,

$$\Delta L_{(c)} = L_{(c)}\varepsilon_{(c)} = \phi_c L\varepsilon_{(c)}, \quad \Delta L_{(a)} = L_{(a)}\varepsilon_{(a)} = \phi_a L\varepsilon_{(a)}. \quad (29)$$

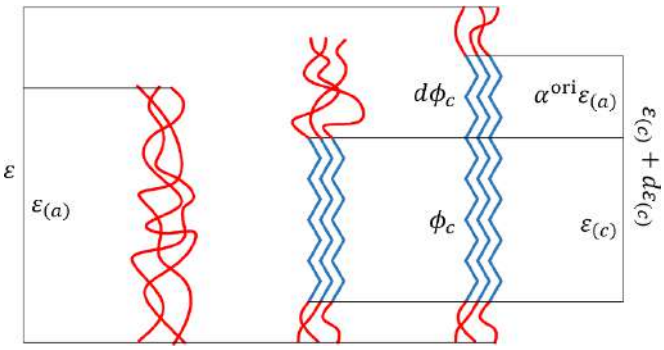

Figure 3. Schematic of cooling elongation caused by chain-packing under 1D deformation. Red parts represent SMP chain segments in amorphous state, and blue parts represent the SMP chain segments in crystalline state.

To demonstrate how the elongation works, consider a situation where $\varepsilon_{(a)}$ is a constant. After a short time interval dt, the increment of ΔL in equation (29) can be expressed as,

$$\mathrm{d}\Delta L = \left(\phi_c \mathrm{d}\varepsilon_{(c)} + \left(\varepsilon_{(c)} - \varepsilon_{(a)}\right)\mathrm{d}\phi_c\right)L. \quad (30)$$

Assuming that the increment length ΔL is proportionate to the length $L_{(a)}$ and increment of phase fraction $d\phi_c$,

$$\mathrm{d}\Delta L = \alpha^{\mathrm{ori}}L_{(a)}\mathrm{d}\phi_c, \quad (31)$$

where α^{ori} is the scale factor.

From equations (29) and (31), the increment strain of crystalline is derived as,

$$\mathrm{d}\varepsilon_{(c)} = \frac{\mathrm{d}\phi_c}{\phi_c}\left(\left(\alpha^{\mathrm{ori}}+1\right)\varepsilon_{(a)} - \varepsilon_{(c)}\right). \quad (32)$$

Then, the solution of equation (32) is,

$$\varepsilon_{(c)} = \left(\alpha^{\mathrm{ori}}+1\right)\varepsilon_{(a)} + \frac{C}{\phi_c}, \quad (33)$$

where C is a constant. To avoid divergence of the solution, $C = 0$ is needed. We obtain the strain of elongation during crystallization as,

$$\varepsilon_{(c)} = \left(\alpha^{\mathrm{ori}}+1\right)\varepsilon_{(a)}. \quad (34)$$

The normal amorphous SMP has $\alpha^{\mathrm{ori}} = 0$, which means that the polymer will not elongate at cooling obtained from equation (31). The thermadapt SMP has a positive α^{ori}, and so it will elongate at stretched cooling.

Generally, the $\varepsilon_{(a)}$ is not a constant in the dynamic crystallization process. Thus, equation (32) is more suitable for the 1D case and can be simplified further as,

$$\mathrm{d}\varepsilon_{(c)} = \frac{\mathrm{d}\phi_c}{\phi_c}\alpha^{\mathrm{ori}}\varepsilon_{(a)}. \quad (35)$$

The above model can be generalized to 3D finite deformation to realize the packing of chains by changing the viscous

deformation rate of the intermolecular branch. A polar decomposition of the network elastic component gives the following:

$$\mathbf{F}^{ne}_{(a)} = \mathbf{V}^{ne}_{(a)}\mathbf{R}^{ne}_{(a)}, \quad \mathbf{F}^{ne}_{(c)} = \mathbf{V}^{ne}_{(c)}\mathbf{R}^{ne}_{(c)}, \tag{36}$$

where $\mathbf{V}^{ne}_{(a)}, \mathbf{V}^{ne}_{(c)}$ are the symmetric tensor and $\mathbf{R}^{ne}_{(a)}, \mathbf{R}^{ne}_{(c)}$ are the orthogonal tensor.

When the polymer is crystallizing, equation (35) becomes,

$$\mathbf{d}^{\text{ori}} = \frac{\dot{\phi}_c}{\phi_c}\alpha^{\text{ori}}\mathbf{V}^{ne}_{(a)}, \quad \left(\dot{\phi}_c > 0\right), \tag{37}$$

where $\mathbf{d}^{\text{ori}}$ is one part of the viscous deformation rate $\mathbf{d}^{mv}_{(c)}$ caused by chain packing. The other part of $\mathbf{d}^{mv}_{(c)}$ cause by viscous flow will be introduced in the next section. The parameter α^{ori} can be obtained from the force-program SMC, after other thermal and mechanical parameters are determined.

When the polymer melts, the crystalline phase melts evenly as observed in the experiment, and the deformation rate $\mathbf{d}^{\text{ori}}$ is,

$$\mathbf{d}^{\text{ori}} = \mathbf{0}, \quad \left(\dot{\phi}_c \leqslant 0\right). \tag{38}$$

2.5. Viscous flow relationship

The viscous deformation rate tensor is usually used to describe viscous flow, and defined from the deformation gradient tensor of the intermediate configuration [27, 30, 31]. Hence, the viscous deformation rates of the four dashpots are defined via their corresponding intermediate configurations, respectively. The viscous deformation rate for the network branches is,

$$\mathbf{d}^{nv}_{(i)} = \text{sym}\left(\dot{\mathbf{F}}^{nv}_{(i)}\left(\mathbf{F}^{nv}_{(i)}\right)^{-1}\right), \tag{39}$$

and for the intermolecular branches is,

$$\mathbf{d}^{mv}_{(i)} = \text{sym}\left(\dot{\mathbf{F}}^{mv}_{(i)}\left(\mathbf{F}^{mv}_{(i)}\right)^{-1}\right), \tag{40}$$

where $\text{sym}(\cdot) = ((\cdot) + (\cdot)^T)/2$ is symmetrization operation.

The viscous deformation rate of the network branches $\mathbf{d}^{nv}_{(i)}$ can be decomposed as,

$$\mathbf{d}^{nv}_{(i)} = \dot{\gamma}^{nv}_{(i)}\mathbf{n}^{n}_{(i)}, \tag{41}$$

where $\dot{\gamma}^{nv}_{(i)}$ is the effective viscous shear stretch rate. $\mathbf{n}^{n}_{(i)}$ indicates the direction of flow, which is the same with the orientation of stress under hypothesis of volume-preserved flow:

$$\mathbf{n}^{n}_{(i)} = \frac{\mathbf{s}^{n}_{(i)}}{\sqrt{\mathbf{s}^{n}_{(i)} : \mathbf{s}^{n}_{(i)}}}. \tag{42}$$

The Arrhenius equation is adopted for the network branch, and the effective viscous flow rate is,

$$\dot{\gamma}^{nv}_{(i)} = \frac{s^{n}_{(i)}}{\eta^{nv}_{\text{ref}}}\exp\left(-\frac{E_0}{k_B T}\right), \tag{43}$$

where $s^{n}_{(i)} = \left(\frac{3}{2}\mathbf{s}^{n}_{(i)} : \mathbf{s}^{n}_{(i)}\right)^{1/2}$ is the effective stress, η^{nv}_{ref} is the reference viscosity of the network branch and E_0 is the activating energy.

Second, intermolecular components have similar decomposition:

$$\mathbf{d}^{mv}_{(a)} = \dot{\gamma}^{mv}_{(a)}\mathbf{n}^{m}_{(a)}, \tag{44}$$

while the crystalline phase has an additional term of elongation in equation (35) under stretching during cooling:

$$\mathbf{d}^{mv}_{(c)} = \dot{\gamma}^{mv}_{(c)}\mathbf{n}^{m}_{(c)} + \mathbf{d}^{\text{ori}}. \tag{45}$$

The direction is similar to equation (42):

$$\mathbf{n}^{m}_{(i)} = \frac{\mathbf{s}^{m}_{(i)}}{\sqrt{\mathbf{s}^{n}_{(i)} : \mathbf{s}^{m}_{(i)}}}. \tag{46}$$

The Williams–Landel–Ferry (WLF) equation is utilized to ascertain the temperature-dependent viscosity of the intermolecular branch:

$$\log_{10}\frac{\eta^{mv}}{\eta^{mv}_{\text{ref}}} = \frac{C_1\left(T - T_g\right)}{C_2 + \left(T - T_g\right)}, \tag{47}$$

where $C_1 = 17.44$ and $C_2 = 51.6\,\text{K}$ are WLF constants and η^{mv}_{ref} is the reference value of viscosity of the intermolecular branch at T_g. The effective viscous flow rate of the intermolecular branch is then obtained:

$$\dot{\gamma}^{mv}_{(i)} = \frac{s^{m}_{(i)}}{\eta^{mv}_{\text{ref}}}\exp\left[-\log 10\frac{C_1\left(T - T_g\right)}{C_2 + \left(T - T_g\right)}\right]. \tag{48}$$

The phase-transition model of reprocessible thermadapt shape memory polymer is summarized in table 1.

3. Validity

To validate the established thermadapt SMP model, the uniaxial stretch performance of this model is analyzed numerically, where the parameters used for our model are listed in table 2. The results are compared with the experiment of Zheng *et al* [15]. The SMC, thermal reprocessing and DMA data used in this study were derived by DMA Q800, and the DSC data were obtained by DSC Q200 (TA instruments).

3.1. Thermodynamic test

As described in section 2.3, the crystallinity at cooling depends not only on the temperature, but also on the cooling rate, especially at the early stage of crystallization. A thermodynamic test under cooling is needed to determine the crystalline parameters. This crystallization can be reflected in the DSC curves

Table 1. Thermo-visco-elastic model.

Kinematics
$\mathbf{F}=\mathbf{F}_{(a)}=\mathbf{F}_{(c)}$
$\mathbf{F}_{(i)}=\mathbf{F}^{M}_{(i)}\mathbf{F}^{\mathrm{th}}_{(i)}$
$\mathbf{F}^{M}_{(i)}=\mathbf{F}^{ne}_{(i)}\mathbf{F}^{nv}_{(i)}=\mathbf{F}^{me}_{(i)}\mathbf{F}^{mv}_{(i)}$
Stress
$\boldsymbol{\sigma}=\phi_a\boldsymbol{\sigma}_{(a)}+\phi_c\boldsymbol{\sigma}_{(c)}$
$\boldsymbol{\sigma}_{(i)}=\mathbf{s}_{(i)}-p_{(i)}\mathbf{I}$
$\mathbf{s}_{(i)}=\frac{\mu^{\mathrm{eq}}}{J_{(i)}}\left(\bar{\mathbf{b}}^{ne}_{(i)}-\frac{1}{3}\bar{I}^{ne}_{(i)}\mathbf{I}\right)+\frac{\mu_i}{J_{(i)}}\left(\bar{\mathbf{b}}^{me}_{(i)}-\frac{1}{3}\bar{I}^{me}_{(i)}\mathbf{I}\right),\quad \mu^{\mathrm{eq}}=Nk_BT\sqrt{n}\frac{\beta_c}{\lambda_c}$
$p=-\frac{\kappa}{J_{(i)}}(J^{M}_{(i)}-1)$
Viscous flow
$\mathbf{d}^{nv}_{(i)}=\dot{\gamma}^{nv}_{(i)}\mathbf{n}^{n}_{(i)},\quad \dot{\gamma}^{nv}_{(i)}=\frac{s^{n}_{(i)}}{\sqrt{2}\eta^{nv}_{\mathrm{ref}}}\exp\left(-\frac{E_0}{k_BT}\right)$
$\mathbf{d}^{mv}_{(a)}=\dot{\gamma}^{mv}_{(a)}\mathbf{n}^{m}_{(a)}$
$\mathbf{d}^{nv}_{(c)}=\dot{\gamma}^{mv}_{(c)}\mathbf{n}^{m}_{(c)}+\mathbf{d}^{\mathrm{ori}}$
$\dot{\gamma}^{mv}_{(i)}=\frac{s^{m}_{(i)}}{\sqrt{2}\eta^{mv}_{\mathrm{ref}}}\exp\left[-\log 10\frac{C_1(T-T_g)}{C_2+T-T_g}\right]$
$\mathbf{d}^{\mathrm{ori}}=\alpha^{\mathrm{ori}}\frac{\dot{\phi}_c}{\phi_c}\mathbf{V}^{n}_{(a)}(\dot{\phi}_c>0),\quad \mathbf{d}^{\mathrm{ori}}=\mathbf{0}(\dot{\phi}_c\leqslant 0)$

Table 2. Parameters.

Parameter	Value	Physical significance
n	5.029×10^{19}	Crosslinking number of unit volume
N	5	Mean number of bonds between two crosslinkings
T_a	12 K	Transition temperature distribution
T_b	304 K	Transition temperature distribution
m	3	Avrami parameters
$K^{\mathrm{av}}_{\mathrm{ref}}$	2.077×10^{-43}	Reference value of Avrami parameters
$T^{\mathrm{av}}_{\mathrm{ref}}$	2.777 K	Reference value of Avrami parameters
α^{r}	$6\times10^{-4}\ \mathrm{K}^{-1}$	Rubbery coefficient of volumetric thermal expansion
α^{c}	$2\times10^{-4}\ \mathrm{K}^{-1}$	Crystalline coefficient of volumetric thermal expansion
E_0	$113.6\ \mathrm{kJ\,mol}^{-1}$	Activating energy
T_g	273 K	Glass transition temperature
η^{mv}_{ref}	1.967×10^{-13} MPa · s	Reference viscosity of intermolecular branch
η^{nv}_{ref}	4.82×10^{3} MPa · s	Reference viscosity of network branch
α^{ori}	0.068	Coefficient of orientation elongation

and DMA results of the following cooling process. The cooling rate of the DSC test was 10 °C/min, and the DMA test was performed at a frequency of 1 Hz with 0.2% strain. The results for DSC and DMA are shown in figures 4(a) and (b), respectively.

Since the crystalline transition is the main reason for the heat absorption of the thermadapt SMP within its working temperature range, the heat absorption condition of its crystalline transition is used to predict the results of the DSC test. Since the heat absorption is proportional to the unit transition volume, the evolution of the crystalline volume fraction of the thermadapt SMP under a specific temperature load is numerically calculated through this model.

In the theoretical model, the storage modulus of the thermadapt SMP is obtained by averaging the storage modulus of each phase weighted by the volume fraction. The storage modulus of each phase can be obtained based on the linearized elastic modulus and viscosity of each element. In addition, through this model, the evolution of the crystalline volume fraction under specific temperature loads can also be numerically calculated. By combining the two, the storage modulus of the DMA test at different temperatures can be predicted.

From the DSC test, a peak at 41 °C exists, which depends on the cooling rate. In the crystallization process, the polymer in the rubber state enters the crystalline state, while transition to the glass state does not occur. The peak of the prediction curve fits well with that of the experimental curve under the same cooling rate. A sharp point exists at 37 °C in the DSC curve, which results from the fact that the Avrami parameters (K^{av}) reach a non-negligible value and that the crystallinity (ϕ_c) rapidly tends to $\phi_{c\infty}$, and so ϕ_c is approximately equal to $\phi_{c\infty}$.

The DMA test shows the relationship between storage modulus and temperature, and the large decrease from 40 °C to 60 °C implies that a phase transition occurs. The modulus at lower and higher temperatures is contributed by crystalline and amorphous phases, respectively. The four-element model fits the transition temperature range well by using the phase transition in the DSC test.

3.2. Relaxation test

Relaxation tests at different temperatures above the reaction temperature are used to obtain the viscosity of network flow

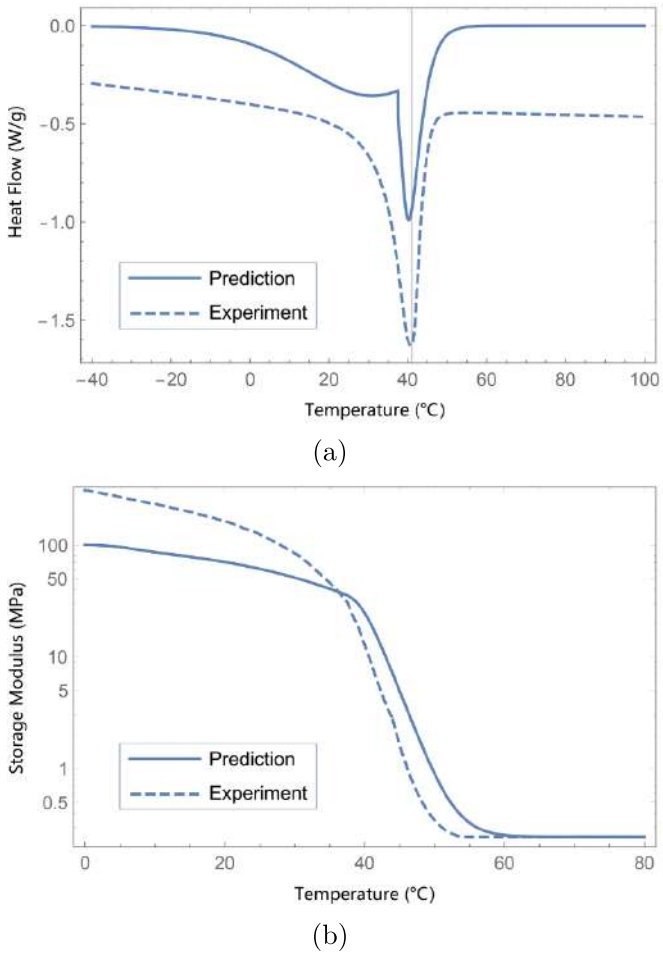

Figure 4. Prediction and experiment of thermodynamic properties, where the solid lines represent the prediction, while the dashed lines represent the experimental results. (a) Results of heat flow versus temperature obtained from our model and the DSC test. (b) Results of storage modulus versus temperature obtained from our model and the DMA test.

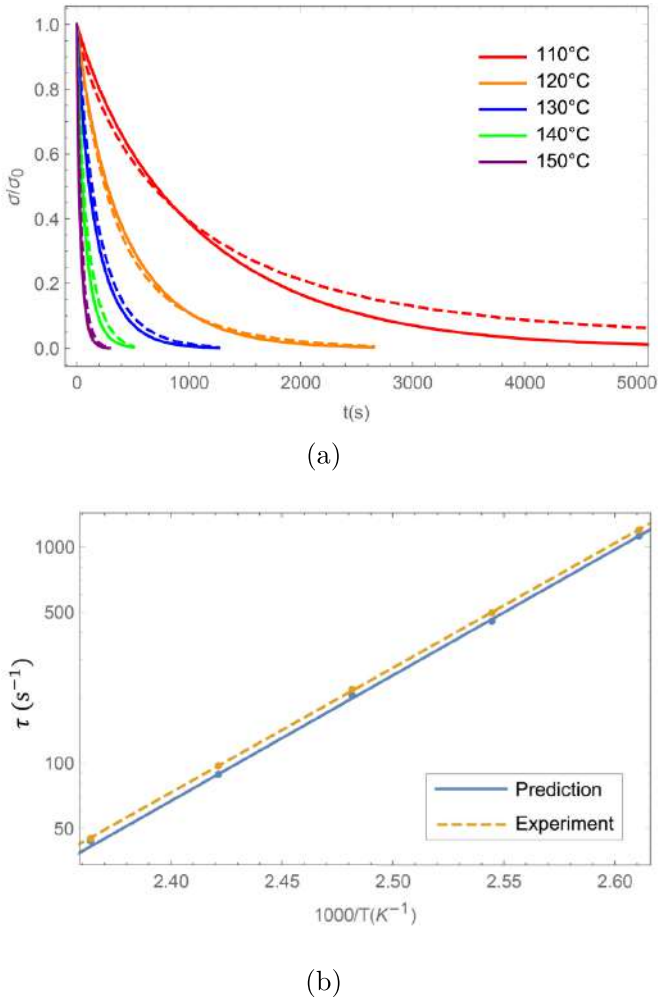

Figure 5. Prediction and experiment of relaxation of SMP under different temperatures. (a) Result of stress changing over time, where the solid lines represent the prediction, while the dashed lines represent the experimental results. Colors of lines represent different temperatures of relaxation. (b) Linear regressive analysis of the Arrhenius equation.

η^{nv}_{ref}. The stress σ relaxation from 110 °C to 150 °C at intervals of 10 °C is predicted numerically by setting the boundary condition of a tensile strain of 0.2% in the stretch direction, and the components of the other stress are 0. In addition, the initial stress is denoted by σ_0.

Figure 5(a) shows the results of relaxation and compares the experimental data with the prediction results of the fitted model. Five groups of tests between 110 °C and 150 °C with equal steps show that the relaxation can be seen as an exponential decay and that the relaxation time descents are also exponential. The curves are transformed to figure 5(b) by experimental fitting, which exhibits superb linearity and validates that the Arrhenius equation is suitable in equation (43). The activating energy E_0 can be obtained from the relaxation test, and then the prediction results are described in figure 5(a). It can be seen that the relaxation curve has a good fitting from 120 °C to 150 °C. Although the relaxation time is a good fit at 110 °C, the predicted stress relaxation behavior is faster than the actual relaxation behavior, indicating that the Arrhenius equation may not apply to low-frequency BER.

3.3. Shape memory cycle

The temperature-dependent mechanical behavior and the stretch-time curve of the SMP in one SMC are shown in figures 6(a) and (b), respectively. One SMC includes four stages: load, shape fixation, unload, shape recovery. At the beginning of the SMC, the thermadapt SMP is in its original shape. The polymer first undergoes a heating process and is programmed into a specific temporary shape under an external load. Next, during the shape fixation stage, the SMP sustains the external load while cooling to room temperature. Consequently, the shape of the SMP is practically fixed. However, due to the continued external load, the third stage of the unloading process sees a minor deformation in the shape of the SMP upon removal of this load, resulting in the final temporary shape. This temporary shape can persist over a long period of time until reheating occurs, marking the final step of the shape recovery process in the SMC. At this

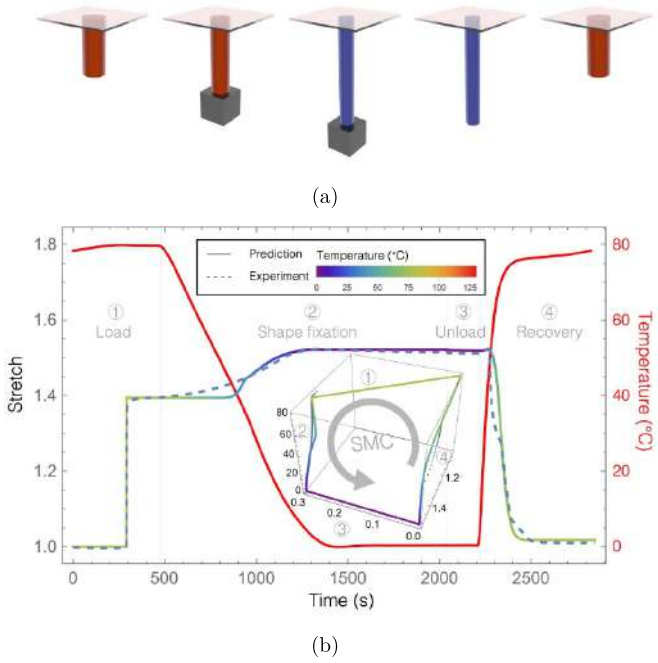

Figure 6. Prediction and experiment of SMC. (a) Schematics of deformation during the whole SMC, where red represents the heated polymer and blue represents the room-temperature polymer. (b) Result of stretch changing over time of an SMC.

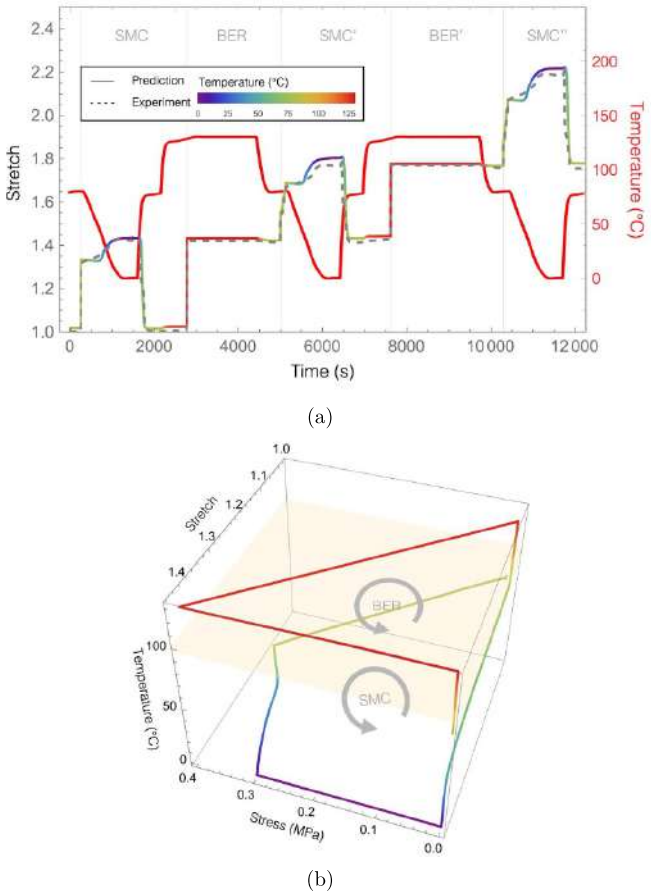

Figure 7. Prediction and experiment of stretch changing over time of three SMCs and three BERs. (a) Prediction and experiment of stretch changing over time. (b) Stress-stretch-temperature relationship in the first SMC and BER.

stage, the heated SMP gradually recovers to its original form, independent of any external load.

It should be noted that crystallization starts after reaching a certain temperature during the heating process, and no such hysteresis is observed during the cooling process, as discussed in section 2.3. The inset in figure 6(b) shows the $\sigma - \lambda - T$ curve after eliminating time. Index 1 to 4 represents the four stages of SMC, including load, shape fixation, unload and shape recovery. The four stages of the curve occur in approximately four planes, which better reflects the characteristics of the SMC.

The thermadapt SMP shows a step at the shape fixation stage under constant force loading, while the curve of a typical SMP is a uniform platform. The step is caused by the polymer chain packing under the stretched cooling discussed in section 2.4.

Figure 7 shows the mechanical behavior of SMP in multiple SMCs with two reprocessed original shapes, demonstrating that the model can predict the experimental values well. The inset in figure 7 shows the $\sigma - \lambda - T$ curve of the first SMC and the first reprocessing after eliminating time.

Compared with the single SMC test, figure 7 includes permanent shape changing. When the shape of the thermadapt SMP is redefined at high temperature (above 100 °C), the polymer network will be rearranged by BER, and then the residual stress of the polymer network will decrease or disappear. If the annealing time is not long enough, the network will retain a certain anisotropy, which will affect the next SMC, and the constitutive model will be able to fit the phenomenon.

In addition, the recovery and fixation rates of SMP are 99% and 98%, respectively, which implies that SMP has an excellent SME during the temperature range of SMC, ensuring that the thermadapt SMP works stably in its working temperature range.

3.4. Smart mandrel application

SMP smart mandrels are a potential manufacturing process of structures with complex surfaces [32–34], where the first and key step is shaping of the smart mandrel. A sealed SMP tube is heated and put into a mold, and then pressure is applied to the inside of the SMP tube. The SMP tube will deform into a predetermined shape. Cooling while preserving pressure, the shape of the smart mandrel can be fixed and used to manufacture the final composite product.

However, shaping a mandrel with angle and small curvature is still a great challenge using the inflation method due to stress concentration, while expansion is necessary to fit the mold. Note that the tube may rupture easily during inflation when manufacturing defects exist, which results in much waste and loss of the advantage of reuse.

Considering an internally inflatable tube shown in figure 8 made of thermadapt SMP, we adopt the same procedure of

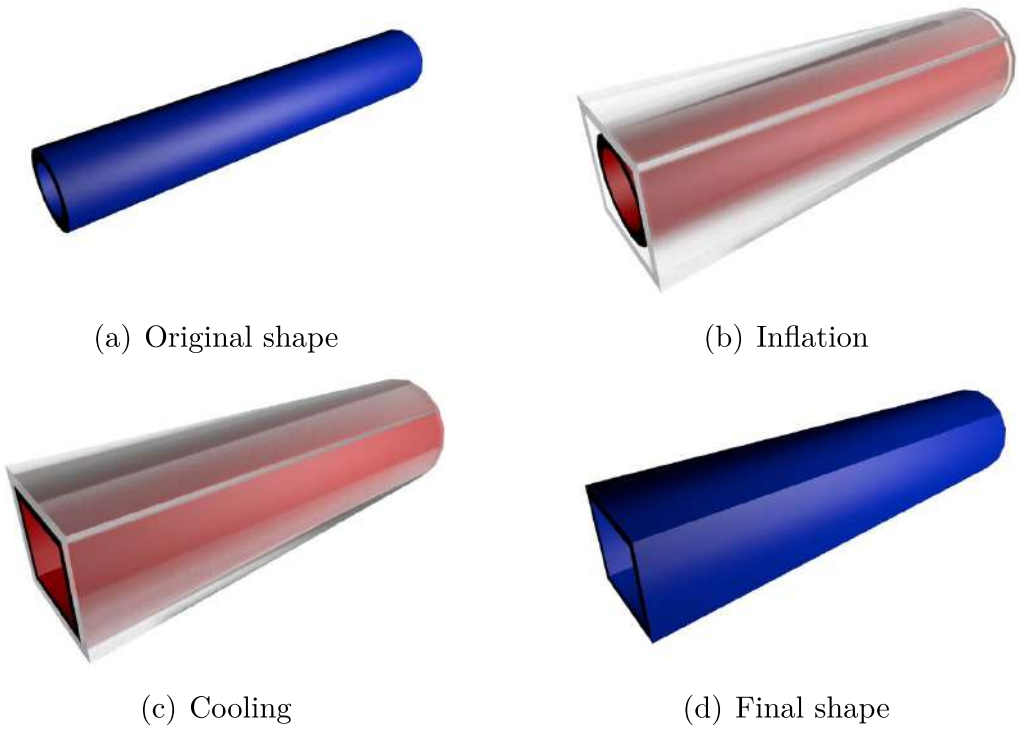

Figure 8. Shaping process of thermadapt SMP mandrel.

using SMP smart mandrels. In the step of heating and inflation, most parts of the tube is contacted with the mold inner wall under inflation pressure, which is much lower than the pressure applied for traditional SMP. Then, keeping the pressure inside the tube and cooling down, the tube surface is under stretch and will self-adaptively expand to fit the small corners and sharp angles of the mold under cooling elongation effect. Thus, lower pressure and self-adaption in processing improve the stress distribution, making the thermadapt SMP a good candidate for smart mandrel.

4. Conclusion

A constitutive model for the processable thermadapt SMP containing crystalline is established, which describes the two-way elongation of the SME and elasticity evolution of reprocessing. The important innovations of this work are summarized as follows. The Avrami equation is reformulated to describe the time-temperature-dependent crystallization process. The equation can be applied to non-constant temperature crystallization processes. A linearized expression is proposed to predict the strain-induced elongation phenomenon of the two-way SME. The equation is interpreted in terms of a packing of stretched polymer atoms. The numerical predictions are compared with the experimental data to validate this model. The results show that the model captures the characteristic temperature of the DSC and DMA analysis. Furthermore, the model can well describe strain-induced elongation, and tensile stiffness changing in the test of SMC, and thermal reprocessing.

This work may potentially guide the design and manufacturing of smart mandrels for thermadapt SMP structures and actuators, especially in predicting the influence of internal stress compatibility on shape changes during thermal-mechanical treatment.

Data availability statement

The data cannot be made publicly available upon publication because they are owned by a third party and the terms of use prevent public distribution. The data that support the findings of this study are available upon reasonable request from the authors.

Acknowledgments

Tong Mu gratefully acknowledges data support from Ning Zheng and Tao Xie. This study was supported by the National Key R&D Program of China (Grant No. 2022YFB3805700).

ORCID iDs

Yanju Liu https://orcid.org/0000-0001-8269-1594
Jinsong Leng https://orcid.org/0000-0001-5098-9871

References

[1] Mu T, Liu L, Lan X, Liu Y and Leng J 2018 Shape memory polymers for composites *Compos. Sci. Technol.* **160** 169–98

[2] Xia Y, He Y, Zhang F, Liu Y and Leng J 2021 A review of shape memory polymers and composites: mechanisms, materials and applications *Adv. Mater.* **33** 2000713

[3] Zhao Q, Jerry Qi H and Xie T 2015 Recent progress in shape memory polymer: new behavior, enabling materials and mechanistic understanding *Prog. Polym. Sci.* **49** 79–120

[4] Leng J, Wu X and Liu Y 2009 Effect of a linear monomer on the thermomechanical properties of epoxy shape-memory polymer *Smart Mater. Struct.* **18** 095031

[5] Liu Z, Mu T, Lan X, Zhao H, Liu L, Bian W, Liu Y and Leng J 2023 Structural and damage analysis of a programmable shape memory locking laminate with large deformation *Composites* B **259** 110755

[6] Lin C, Lv J, Li Y, Zhang F, Li J, Liu Y, Liu L and Leng J 2019 4D-printed biodegradable and remotely controllable shape memory occlusion devices *Adv. Funct. Mater.* **29** 1906569

[7] Xie T and Rousseau I A 2009 Facile tailoring of thermal transition temperatures of epoxy shape memory polymers *Polymer* **50** 1852–6

[8] Li J, Rodgers W R and Xie T 2011 Semi-crystalline two-way shape memory elastomer *Polymer* **52** 5320–5

[9] Behl M, Kratz K, Zotzmann J, Nöchel U and Lendlein A 2013 Reversible bidirectional shape-memory polymers *Adv. Mater.* **25** 4466–9

[10] Pandini S, Baldi F, Paderni K, Messori M, Toselli M, Pilati F, Gianoncelli A, Brisotto M, Bontempi E and Ricco T 2013 One-way and two-way shape memory behaviour of semi-crystalline networks based on sol–gel cross-linked poly (ε-caprolactone) *Polymer* **54** 4253–65

[11] Jin B, Song H, Jiang R, Song J, Zhao Q and Xie T 2018 Programming a crystalline shape memory polymer network with thermo-and photo-reversible bonds toward a single-component soft robot *Sci. Adv.* **4** eaao3865

[12] Jin Y, Yu C, Denman R J and Zhang W 2013 Recent advances in dynamic covalent chemistry *Chem. Soc. Rev.* **42** 6634–54

[13] Zheng N and Xie T 2017 Thermadapt shape memory polymer *Acta Polym. Sin.* **11** 1715–24

[14] Zhang H, Cui J, Hu G and Zhang B 2022 Recycling strategies for vitrimers *Int. J. Smart Nano Mater.* **13** 367–90

[15] Zheng N, Fang Z, Zou W, Zhao Q and Xie T 2016 Thermoset shape-memory polyurethane with intrinsic plasticity enabled by transcarbamoylation *Angew. Chem.* **128** 11593–7

[16] Ma J, Mu X, Bowman C N, Sun Y, Dunn M L, Jerry Qi H and Fang D 2014 A photoviscoplastic model for photoactivated covalent adaptive networks *J. Mech. Phys. Solids* **70** 84–103

[17] Yu K, Shi Q, Li H, Jabour J, Yang H, Dunn M L, Wang T and Qi H J 2016 Interfacial welding of dynamic covalent network polymers *J. Mech. Phys. Solids* **94** 1–17

[18] Liu Y, Gall K, Dunn M L, Greenberg A R and Diani J 2006 Thermomechanics of shape memory polymers: uniaxial experiments and constitutive modeling *Int. J. Plast.* **22** 279–313

[19] Chen Y-C and Lagoudas D C 2008 A constitutive theory for shape memory polymers. Part I: large deformations *J. Mech. Phys. Solids* **56** 1752–65

[20] Qi H J, Nguyen T D, Castro F, Yakacki C M and Shandas R 2008 Finite deformation thermo-mechanical behavior of thermally induced shape memory polymers *J. Mech. Phys. Solids* **56** 1730–51

[21] Reese S, Böl M and Christ D 2010 Finite element-based multi-phase modelling of shape memory polymer stents *Comput. Methods Appl. Mech. Eng.* **199** 1276–86

[22] Barot G and Rao I J 2006 Constitutive modeling of the mechanics associated with crystallizable shape memory polymers *Z. Angew. Math. Phys.* **57** 652–81

[23] Barot G, Rao I J and Rajagopal K R 2008 A thermodynamic framework for the modeling of crystallizable shape memory polymers *Int. J. Eng. Sci.* **46** 325–51

[24] Hall R B, Rao I J and Qi H J 2014 Thermodynamics and thermal decomposition for shape memory effects with crystallization based on dissipation and logarithmic strain *Mech. Time-Depend. Mater.* **18** 437–52

[25] Westbrook K K, Parakh V, Chung T, Mather P T, Wan L C, Dunn M L and Qi H J 2010 Constitutive modeling of shape memory effects in semicrystalline polymers with stretch induced crystallization *J. Eng. Mater. Technol.* **132** 041010

[26] Arruda E M and Boyce M C 1993 A three-dimensional constitutive model for the large stretch behavior of rubber elastic materials *J. Mech. Phys. Solids* **41** 389–412

[27] Nguyen T D, Qi H J, Castro F and Long K N 2008 A thermoviscoelastic model for amorphous shape memory polymers: incorporating structural and stress relaxation *J. Mech. Phys. Solids* **56** 2792–814

[28] Doufas A K, McHugh A J and Miller C 2000 Simulation of melt spinning including flow-induced crystallization: Part i. model development and predictions *J. Non-Newton. Fluid Mech.* **92** 27–66

[29] Ahzi S, Makradi A, Gregory R V and Edie D D 2003 Modeling of deformation behavior and strain-induced crystallization in poly (ethylene terephthalate) above the glass transition temperature *Mech. Mater.* **35** 1139–48

[30] Diani J, Liu Y and Gall K 2006 Finite strain 3D thermoviscoelastic constitutive model for shape memory polymers *Polym. Eng. Sci.* **46** 486–92

[31] Nguyen T D, Yakacki C M, Brahmbhatt P D and Chambers M L 2010 Modeling the relaxation mechanisms of amorphous shape memory polymers *Adv. Mater.* **22** 3411–23

[32] Everhart M C, Nickerson D M and Hreha R D 2006 High-temperature reusable shape memory polymer mandrels *Smart Structures and Materials 2006: Industrial and Commercial Applications of Smart Structures Technologies* vol 6171 (SPIE) pp 178–87

[33] Du H, Liu L, Leng J, Peng H, Scarpa F and Liu Y 2015 Shape memory polymer s-shaped mandrel for composite air duct manufacturing *Compos. Struct.* **133** 930–8

[34] Du H, Liu L, Zhang F, Leng J and Liu Y 2018 Shape retainability and reusability investigation of bottle-shaped smp mandrel *Polym. Test.* **69** 325–31